


## Differential cross sections of the $^{16}\text{O}(n, \alpha)$ reaction at neutron energies from 3.8 to 15 MeV

H. Y. Lee <sup>\*</sup>, S. A. Kuvin, L. Zavorka <sup>†</sup>, S. Mosby, B. DiGiovine , G. Hale, M. Paris , D. Votaw <sup>‡</sup> and M. White   
 Los Alamos National Laboratory, Los Alamos, New Mexico 87545, USA

 (Received 17 February 2023; revised 28 July 2023; accepted 23 October 2023; published 2 January 2024)

The importance of studying the  $^{16}\text{O}(n, \alpha)$  reaction is motivated by multiple nuclear applications which rely on an accurate nuclear reaction data library for oxygen. Discrepancies between past experimental data on the  $^{16}\text{O}(n, \alpha)^{13}\text{C}$  reaction and its time-reverse  $^{13}\text{C}(\alpha, n)^{16}\text{O}$  reaction have led to various different nuclear data evaluations. We have measured  $^{16}\text{O}(n, \alpha)$  reaction cross sections using the LENZ instrument with the unmoderated white neutron source at LANSCE. Results from 2016/2017 data are discussed and used to benchmark the MCNP and GEANT simulations of the LENZ experimental setup. We report partial differential cross sections of  $^{16}\text{O}(n, \alpha_0)$  at  $E_n = 3.8\text{--}15$  MeV and  $^{16}\text{O}(n, \alpha_1 + \alpha_2 + \alpha_3)$  at  $E_n = 9\text{--}15$  MeV, based on the new measurement in 2021. The resonances that we observed are in good agreement with the levels in  $^{17}\text{O}$  that were previously measured. The LENZ cross sections are in better agreement with the ENDF/B-VIII.0 evaluation than the with reduced cross section found in ENDF/B-VII.1 up to 6 MeV. However, the current results for  $^{16}\text{O}(n, \alpha_0)^{13}\text{C}_{\text{g.s.}}$  appear to be in the best agreement over the entire energy range with that of JENDL/AN-2005 (ENDF/B-VI.0).

DOI: [10.1103/PhysRevC.109.014601](https://doi.org/10.1103/PhysRevC.109.014601)

### I. INTRODUCTION

Oxygen is pervasive in our environment and present in air, water, various oxides, concrete and elsewhere. Many nuclear applications are highly sensitive to the uncertainties in the oxygen nuclear reaction data libraries. These applications include informing reactor designs through understanding neutron reactivity in oxide fuels, solution data testing to benchmark critical assemblies, manganese bath experiments to deduce neutron fluence, understanding radiobiology due to the oxygen content in biological systems, and more. Neutron-absorption reactions, like  $(n, \alpha)$ , reduce the amount of available neutrons in such applications and, therefore, precise knowledge of neutron-induced reactions on oxygen is necessary. As the largest neutron induced reaction cross section besides elastic scattering in the energy range relevant for the prompt fission neutron spectrum (PFNS), Fig. 1 shows the current status of available evaluations for the  $^{16}\text{O}(n, \alpha)$  reaction. Different releases of the ENDF/B library (VI.8 [1], VII.1 [2], and VIII.0 [3]) present substantial discrepancies in cross sections over the neutron energy range of interest, and it is noted that the latest JEFF3.3 [4] and JENDL4.0 [5] evaluations are very similar to ENDF/B-VI.8, so they are omitted in this comparison. JENDL/AN 2005 [6] was the evaluation of neutron emission data for the  $(\alpha, xn)$  reactions, so the  $^{13}\text{C}(\alpha, n_0)$  reaction was used for deducing the  $^{16}\text{O}(n, \alpha)$  cross section by applying detailed balance. Therefore, the Collaborative International Evaluated Library Organization

(CIELO) project [7] had a motivation of reconciling these discrepancies and settling on a best value [8], and concluded the need of new, independent measurements for confirmation [9,10].

At the heart of the question on the  $^{16}\text{O}(n, \alpha)^{13}\text{C}$  reaction cross section is the 30–50% discrepancy among previous measurements. Figure 2 shows the subset of cross sections taken from Experimental Nuclear Reaction Data (EXFOR [11]). Experimental data were obtained via two different reaction methods. One approach is to directly measure the  $^{16}\text{O}(n, \alpha)$  reaction [7,8,12,13]. Gas detectors like a Frisch-gridded ionization counter or a proportional counter were used with a gas mixture that contained oxygen as an active target and detected reaction  $\alpha$ 's to deduce the  $^{16}\text{O}(n, \alpha)^{13}\text{C}$  cross section. Since the target gas plays as a counting gas as well, identifying reaction  $\alpha$  signals from background noise is critical to determine reaction yields during data analyses. A common method is to subtract out the background contribution by measuring the yield without oxygen in gas; however, this could be incomplete or complex due to the difficulty of duplicating the exact same detection condition as the foreground measurement. While using gas detectors, another difficulty lies in accurately estimating an angular coverage and a detection efficiency, which can be different from a geometric efficiency, due to the small pulse-height signal's nonlinearity relative to the incoming energy and the detection threshold, and the nonuniform electric field near edges of the detection volume. Conventionally, neutron beams were produced via charged particle reactions with a gas target such as  $^3\text{H}(p, n)$ ,  $^2\text{H}(d, n)$ , or  $^2\text{H}(t, n)$  reactions, resulting in significant energy broadening at the gas cell's window as discussed in the previous  $(n, \alpha)$  measurements [7,8]. Therefore, systematic uncertainties of using a gas detector are heavily dependent

<sup>\*</sup>Corresponding author: [hylee@lanl.gov](mailto:hylee@lanl.gov)

<sup>†</sup>Present address: Oak Ridge National Laboratory, Oak Ridge, TN.

<sup>‡</sup>Present address: U.S. Department of Defense, Washington, DC.

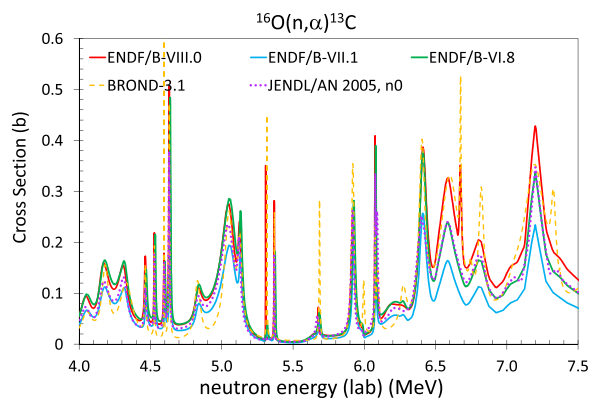


FIG. 1. Current status of available evaluations for the  $^{16}\text{O}(n, \alpha)$  reaction. JEFF3.3 and JENDL4.0 are very similar to ENDF/B-VI.8, so they are omitted in this comparison.

on individual experiment's configurations and data analysis methods.

At the Institute of Nuclear Physics and Power Engineering (IPPE) in Russia, authors [8] reported the neutron energy range of 1.7–7 MeV, with neutron energy resolutions in FWHM varying as 180 keV at 5 MeV, 138 keV at 6 MeV, and 114 keV at 7 MeV. At the Institute for Reference Materials and Measurements (IRMM) in Belgium, the reported neutron energy resolutions were 121 keV at 5 MeV, 98 keV at 6 MeV, and 83 keV at 7 MeV [7], while individual systematic uncertainties were reported as 2.5% for estimating the number of oxygen nuclei in the gaseous target and 3.6–4.4% for estimating number of reaction and monitor events, resulting in an overall uncertainty of 6.6% after combining with about 5% statistical uncertainty. The recent  $(n, \alpha)$  reaction measurement [14] used the similar setup as Refs. [7,8] at IPPE and reported a total systematic of 6.8%, including uncertainties estimating for a target thickness with 4%, a detector efficiency with 4%, a beam current with 2%, solid angles with 2.5%, and multiple scattering corrections with 2%. Davis *et al.* [12] reported the neutron energy resolution varying from 25 keV at 5.0 MeV and 50 keV at 8.5 MeV, while the final uncertainty ranged from 20% at 5 MeV to 30% at 8.7 MeV for  $(n, \alpha_0)$  and up to 50% for  $(n, \alpha_{2+3})$  due to background corrections, the determination of the absolute neutron flux, and counting statistics and adding the counts in each group of the pulse-height distribution.

The other approach is to measure the time-reverse reaction,  $^{13}\text{C}(\alpha, n)^{16}\text{O}$  [15–18], to deduce the  $^{16}\text{O}(n, \alpha)$  cross section using the reciprocity theorem. As  $\alpha$ 's are used as a beam, the reaction mechanism produces  $(\alpha_0, n_{0,1,2,3,\dots})$ , whereas the  $^{16}\text{O}(n, \alpha)$  reaction produces  $(n_0, \alpha_{0,1,2,3,\dots})$ . Therefore, different sets of excited states are populated between forward and reverse reactions at high energies. The reaction is measured by impinging an  $\alpha$  beam on a  $^{13}\text{C}$  target, followed by detection of emitted neutrons in a neutron detection array, which is composed of individual scintillator detectors for differential energy-angle information or of  $^3\text{He}$  or  $\text{BF}_3$  counters inside a moderator for angle-integrated detection. In order to compensate for decreasing cross sections at low energies, a thick target (several times thicker than resolved resonance widths)

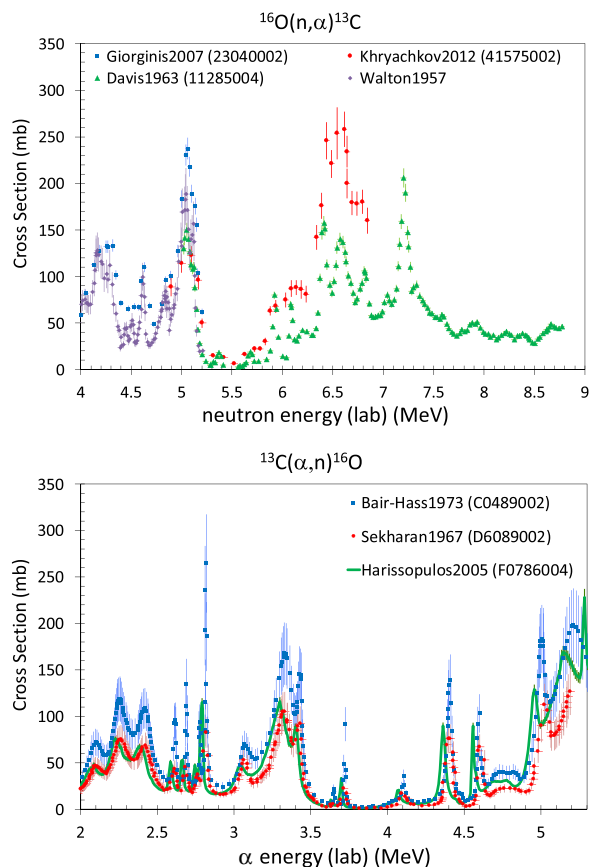


FIG. 2. Subset of available experimental data performed on the  $^{16}\text{O}(n, \alpha)$  reaction (top) and the reverse  $^{13}\text{C}(\alpha, n)$  reaction (bottom) retrieved from EXFOR [11]. The number in the parenthesis of the legend corresponds to the EXFOR subentry number. The Walton1957 data were taken from Ref. [13].

was often used and the beam energy has to be corrected for effective alpha energies. For the  $^{13}\text{C}$  target thickness, Bair and Hass [15] reported the measured thickness of 5 keV at  $E_\alpha = 1$  MeV and Harissopolos *et al.* [17] reported the measured thickness of 31 keV at  $E_\alpha = 3$  MeV. A neutron detector efficiency was determined by simulating response functions, which were then calibrated against well known references. Bair and Hass [15] used a Sb-Be source to calibrate their neutron detectors. Sekharan [16] used the  $^7\text{Li}(p, n)$  reaction to calibrate at multiple neutron energies and a Ra- $\alpha$ -Be source to extend the energy up to 5 MeV. Harissopolos *et al.* [17] used a  $^{252}\text{Cf}$  spontaneous fission source, of which PFNS has a shape of the Maxwellian distribution with the temperature of 1.42 MeV and the mean energy peaks at around 2 MeV, as discussed in Ref. [19]. PFNS might not be an optimal reference for calibrating neutrons above 4 MeV, where fission neutron becomes scarce. In addition, the relevant neutron energy from this  $^{13}\text{C}(\alpha, n)$  reaction ranges from 3.5 to 9.0 MeV. The neutron detection systems that were used for these measurements, including moderator with  $\text{BF}_3$  or  $^3\text{He}$  counters, have efficiencies that depend on neutron energy and emission angle. This dependence of the efficiency on neutron energy and emission angle needs to be investigated with Monte Carlo

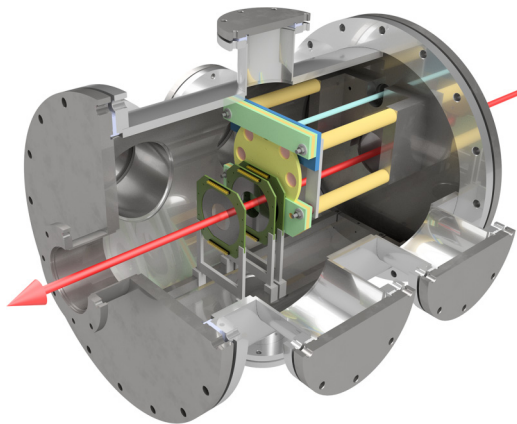


FIG. 3. LENZ instrument with DSSD detectors positioned to detect outgoing  $\alpha$  particles at forward angles in the 2016 experimental setup.

simulations. Both Bair and Hass [15] and Sekharan *et al.* [16] reported their total cross-section uncertainties to be 20%, whereas Harissopoulos *et al.* [17] reported 4% as the total uncertainty.

Recent studies [20,21] have shown that the overall normalization of Harissopoulos *et al.* may require a correction as large as 15–37%, well outside the uncertainties quoted in the original measurement. Meanwhile, similar analyses applied to the Bair and Haas data typically renormalize the overall scale of the cross section to be reduced by between 8–20%, which is well within their quoted uncertainty. In addition, Refs. [22] and [23] highlight an unaccounted source of systematic uncertainty in the Harissopoulos measurement, at energies above 5 MeV, due to making an assumption that the total cross section is dominated by the  $(\alpha, n_0)$  contribution only and neglecting the potential contributions from other open channels  $(\alpha, n_1)$ ,  $(\alpha, n_2)$ , etc. The Bair and Haas experimental setup is less sensitive to this effect because the neutron detection efficiency over the relevant neutron energy range is reported to be less energy dependent than that of the Harissopoulos measurement. Regardless, the open  $(\alpha, n)$  channels that do not lead to the ground state of  $^{16}\text{O}$  present a technical complication in using the total  $^{13}\text{C}(\alpha, n)$  cross section data to determine the  $^{16}\text{O}(n, \alpha_0)$  cross section. As an example, the very narrow resonance that is prevalent in Fig. 1 between the 6.56 and 6.8 MeV resonances in ENDF/B-VIII.0 and BROND-3.1 but not found in ENDF/B-VI.8 or B-VII.1 is likely due to the contribution of  $^{13}\text{C}(\alpha, n_2)$  as shown in Fig. 2 of Febraro *et al.* [24] and Fig. 11 of deBoer *et al.* [25]. Hence, this narrow resonance contribution to the total  $^{13}\text{C}(\alpha, n)$  cross section may not have been properly subtracted when using  $^{13}\text{C}(\alpha, n_0)$  to derive  $^{16}\text{O}(n, \alpha_0)$ .

Finally, it is worth noting that the reduced scale of ENDF/B-VII was set based on the reported high precision of the Harissopoulos data and explicitly treating the Bair and Haas data as being unreliable. However, it is obvious from the recent studies on the Harissopoulos data's unaccounted systematic uncertainty that the data should bring the final uncertainty to be more on par with that of the Bair and Haas data (e.g.,  $\approx 20\%$  instead of 4%). By adopting this uncertainty, the scales

of the two data sets are in better agreement, and the approach to completely exclude the Bair and Haas data is definitely not warranted.

## II. $^{16}\text{O}(n, \alpha)$ MEASUREMENTS AT LANSCE

In order to enhance the fidelity of new measurements, the desired requirements would be (a) a well characterized setup, with a large number of target atoms and a detection system with a high efficiency and a known response function, (b) a high signal-to-background ratio and low detection threshold to detect low-energy  $\alpha$ 's, (c) good energy resolutions for neutrons and  $\alpha$ 's to resolve narrow resonances, (d) improved systematic uncertainty over a broad energy range to reconcile the discrepancy among experimental cross sections, and (e) additional angular distributions for the resonance analysis with advanced *R*-matrix codes [26–29].

### A. LENZ (Low Energy NZ) instrument

At LANSCE, neutrons are produced in the energy range from thermal to several hundred MeV using two different spallation neutron sources [30]. At the Weapons Neutron Research (WNR) facility, an 800-MeV proton impinges a bare tungsten target (T4), producing fast neutrons as a white spectrum. Protons are pulsed to have the time structure of the 1.8  $\mu\text{s}$  repetition rate, so the neutron energy is determined by measuring a time stamp of the detected neutron or the neutron-induced reaction product relative to the proton time stamp (called T0), which is a pickoff signal of the proton right before bombarding T4.

The LENZ instrument [31–33] is an upgrade of the preceding NZ chamber [34–36] at WNR, which has been used to measure cross sections of neutron-induced charged particle reactions up to 50 MeV. The LENZ instrument is designed for large solid-angle coverage and low detection threshold to measure  $\alpha$ 's efficiently. The cut-through rendered image of LENZ is shown in Fig. 3. The target wheel can hold up to eight different targets at once, including the targets of interest, a backing material, a calibration source, a flux reference target, etc. Double-sided silicon strip detectors (DSSDs) are used with various thicknesses of two different types: S1 type detectors (an active area is defined by the disk of the 48 mm outer radius with the hole of the 24 mm inner radius) and S3 detectors (an active area is defined by the disk of the 35 mm outer radius with the hole of the 11 mm inner radius) [37]. Using customized printed circuit board (PCB) adapters, both detector types provide 16 annular segmentations on the front for determining  $\theta$  angles and 16 azimuthal segmentations on the back for determining  $\phi$  angles. Signals are fed into the Mesytec charge integrating preamplifier MPR-16L [38] and the output signals are processed with the CAEN V1730, which is a 16-channel 14-bit 500 MS/s flash analog to digital converter (ADC) waveform digitizer [39]. The specification of the electronics settings and the waveform analysis utilizing the pulse shape discrimination (PSD) method are discussed in the LENZ instrumentation paper [31]. The location of these DSSDs was optimized for large solid angle coverage in the 2016 LENZ data as displayed in Fig. 3. The DSSD detec-

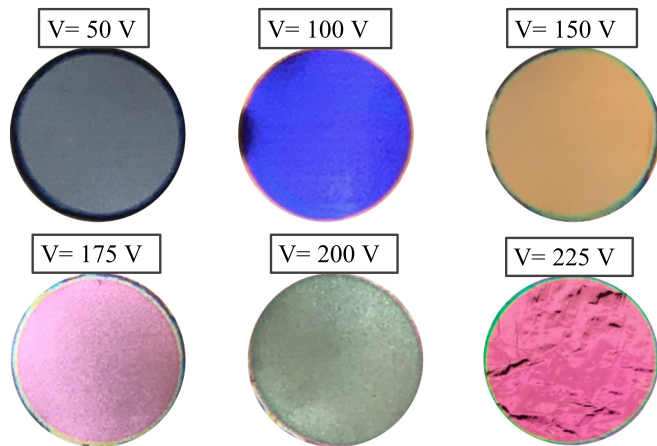


FIG. 4. Picture of  $\text{Ta}_2\text{O}_5$  targets that were manufactured by the anodizing technique on  $30\ \mu\text{m}$  thick Ta backings, except the  $V = 225\ \text{V}$  one on a  $3\ \mu\text{m}$  thick Ta, to reduce beam-induced backgrounds. The voltages shown on each picture are the anodization voltages, corresponding to different optical colors.

tor's intrinsic response function of geometric efficiency and resolution was simulated using the GEANT4 simulation code [40]. The  $^{229}\text{Th}$   $\alpha$  calibration source and multiple reference reactions were used to validate the GEANT4 simulation with the LENZ measurement, which showed good agreement. The details of the LENZ GEANT4 work can be found in Ref. [41].

### B. Solid oxygen target fabrication and characterization

The improvement on targets was made by fabricating solid oxygen targets to reduce systematic uncertainties associated with the gaseous oxygen quantity and detection efficiency, as addressed in Sec. I. We used two types of solid oxygen target. One was to use  $\text{Ta}_2\text{O}_5$  targets via the anodizing technique of applying an electric field in water to etch oxygen ions onto tantalum substrates [42]. The other was to use a mylar foil in the form of  $\text{C}_{10}\text{H}_8\text{O}_4$ , which provided reference reaction yields from carbon and hydrogen.

For the anodizing technique, the different target thickness was achieved by applying different voltages from 50 to 250 V, which corresponded to different optical colors as shown in Fig. 4. Some systematic uncertainties associated with the anodizing technique were adopted from the previous works [43–46]. For the relationship between the voltage applied and the final  $\text{Ta}_2\text{O}_5$  thickness, a small variation of about  $\pm 0.8\ \text{nm}$  [42] for the thickness range of 250–500 nm, relevant for this work, was reported because of observed variations in current density, temperature, and applied voltages during fabrication. For the absolute oxygen thickness, it was reported to be about 2% via six laboratories' independent measurements [45] using (1) nuclear reaction analysis (NRA) via the  $^{16}\text{O}(d, p_1)^{17}\text{O}^*$  reaction, (2) Rutherford backscattering analysis, and (3) elastic recoil detection analysis. In addition, this robust and independent work reported the stoichiometry uncertainty being about 2.5% in terms of the constant stoichiometry and the long-term stability. For the same anodizing setup used to fabricate the 2016/2017 targets in this work

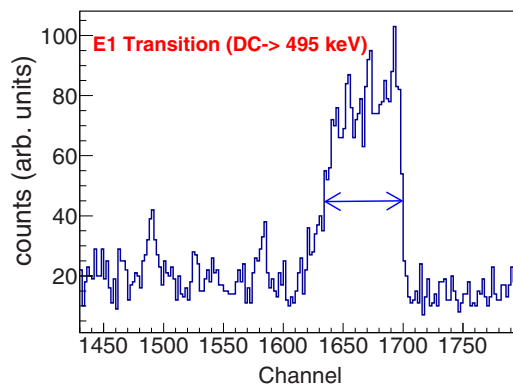


FIG. 5.  $\gamma$ -ray spectrum of the  $^{16}\text{O}(p, \gamma)^{17}\text{F}$  reaction obtained with a HPGe detector using the anodized  $\text{Ta}_2\text{O}_5$  target. The peak was obtained by detecting  $E_\gamma = 1.04\ \text{MeV}$  and the arrow in the width represented the target thickness of  $400\ \text{nm}$ , which was used in 2016/2017 measurement campaigns. Details of the method is discussed in Sect. II B.

(details are summarized in Table I), the oxygen thickness was calibrated from the initial reference formula [42], using NRA with  $\alpha$  beams at  $1.0\ \text{MeV}$  [43] and at  $2.5\ \text{MeV}$  [46], resulting in the final target thickness uncertainty of 5%, including uncertainties of the stopping powers taken from SRIM (3%) [46]. The thickness of the same target was observed to differ by 4% between the  $R$ -matrix analysis and NRA [43].

The first batch of anodized  $\text{Ta}_2\text{O}_5$  targets used for 2016/2017 measurement campaigns was characterized to confirm the thickness of the oxygen deposit via measuring  $\gamma$  rays from the  $^{16}\text{O}(p, \gamma)^{17}\text{F}$  reaction, since the observed peak width of the direct-capture transitions to bound states is dependent on the target thickness [47]. The 5 MV single-ended Pelletron at the University of Notre Dame was used to provide a proton beam at  $990\ \text{keV}$ , after being calibrated with a well-known resonance of  $E_p = 992\ \text{keV}$  from the  $^{27}\text{Al}(p, \gamma)$  reaction. One 65% high-purity germanium (HPGe) detector was positioned at the angle of  $135^\circ$  relative to the proton beam to measure the  $1.038\text{-MeV}$   $\gamma$  transition to the first excited state in  $^{17}\text{F}$  ( $E_{\text{ex}} = 495\ \text{keV}$ ,  $J^\pi = 1/2^+$ ) following the proton capture at  $E_p = 990\ \text{keV}$ . The measured  $\gamma$ -ray spectrum is shown in Fig. 5, confirming about  $400\ \text{nm}$  thickness and  $2.2 \times 10^{18}$  oxygen atoms/ $\text{cm}^2$  with the stopping power and the range obtained from the SRIM calculation [48]. The final uncertainty for determining the target thickness was 3%, after combining uncertainties from SRIM calculations, counting statistics, measurements with different thicknesses, and independent relative confirmation of the thickness with a mylar foil, which will be discussed below. The uniformity of targets was optically inspected with the areal survey using scanning electron microscopy. Targets used in the 2021 data were fabricated using a new Los Alamos National Laboratory (LANL) anodizing setup, and the target thickness was confirmed relatively to the targets used in 2016/2017 campaigns.

The other solid oxygen target, a mylar foil,  $\text{C}_{10}\text{H}_8\text{O}_4$ , has a thickness of  $1.6\ \mu\text{m}$  with known stoichiometry and this target contains hydrogen and carbon, of which cross sections are neutron standards. A relative measurement to the reaction



TABLE I. LANSCE data sets.

Run cycle (year)	Beam size radius (cm)	Target (thickness) (Ta <sub>2</sub> O <sub>5</sub> /Ta backing)	Detector thickness (μm)	Detector's distance from target (cm)	Nominal angles (degrees)	Vac. window material
2016	1	Ta <sub>2</sub> O <sub>5</sub> (400 nm/125 μm)	71 & 1000	3.9 & 7.0	19°–51°	Kapton
2017	1	Ta <sub>2</sub> O <sub>5</sub> (400 nm/125 μm)	300 & 500	4.1 & 9.1	15°–50°	Kapton
2021	0.5	Mylar: C <sub>10</sub> H <sub>8</sub> O <sub>4</sub> (1.6 μm)	300, 300	20 & 12.5, –2.5	7°–21°, 124°–142°	Al. alloy
2021	0.5	Ta <sub>2</sub> O <sub>5</sub> (350 & 500 nm/3 μm)	300, 300	12.5 & 2.5	11°–21°, 44°–63°	Al. alloy

with better-known cross sections, called the ratio method, was performed to reduce the uncertainties associated with the estimate of the beam flux, the detection efficiency, the target uniformity, and the target thickness, as long as the stoichiometry was known and stable during irradiation. For the mylar target, the cross section of the  $^{16}\text{O}(n, \alpha)$  reaction was measured as ratios to those of  $^1\text{H}(n, \text{el})$  and  $^{12}\text{C}(n, \alpha)$ . This ratio method relative to  $^1\text{H}(n, \text{el})$  is independent of the absolute oxygen target thickness and constrains the overall uncertainty for the configuration with detector positions at very forward angles where the proton recoils can be cleanly identified. Details of uncertainties from the ratio method will be discussed in Sec. II G.

### C. Neutron flux measurement at WNR flight path 15R

The 15R flight path has the neutron flight length of 13–28 meters from WNR T4 and is angled at 15° to the proton-beam right direction. The neutron flux at the flight path is continuously monitored by measuring fission fragments in a fission counter [49,50]. The  $^{238}\text{U}$  actinide was deposited on a backing foil with a thickness of 0.678 mg/cm<sup>2</sup> for an atom density of  $3.68 \times 10^{17}$  atoms/cm<sup>2</sup>. The fission counter was positioned at the flight path length of 13.407 m from T4. The neutron fluxes in front of the LENZ instrument and behind LENZ have been measured, confirming negligible distortion in the absolute flux and spectrum. The uniformity of the neutron beam was confirmed by taking beam images at the target position. The measured neutron flux is in good agreement with the MCNP calculation [51] that simulated the WNR T4 spallation production and the neutron transport at the fission counter in flight path 15R. Further flux estimates from 3 to 10 MeV, the relevant energy for  $^{16}\text{O}(n, \alpha)$ , and associated uncertainties will be discussed in Sec. II G.

### D. $^{16}\text{O}(n, \alpha)$ reaction measurements in 2016/2017

The  $^{16}\text{O}(n, \alpha)$  reaction measurements were performed in the LANSCE run cycles in 2016, 2017, and 2021. Each experimental configuration is summarized in Table I. Based on the availability of silicon strip detectors and the optimization of solid angle coverage, LENZ configurations were complementary to cover a broad range of solid angles. Detecting  $\alpha$ 's at backward angles ( $>90^\circ$ ) was not favored, due to energy and angle straggling and smaller outgoing energies due to kinematics, therefore silicon detectors were only positioned at forward angles in 2016 and 2017. However, with the optimized experimental configuration in 2021, differential cross

sections at backward angles were also obtained with the mylar target.

Annular segmentations in the DSSD were used to estimate the charged particle's detected angle in the laboratory system,  $\theta$ , by assuming the reaction locus was from the center of the target, labeled as the “nominal angle” in Fig. 6. However, the extended neutron beam spot of  $\approx 2$  cm in diameter during 2016 and 2017 runs resulted in actual emitting angles in the range from “ $\theta_1$ : minimum angle” to “ $\theta_2$ : maximum angle” as shown in Fig. 6. The time of flight (TOF) of the charged particle is converted to the incoming neutron energy after correcting for the charged particle's travel time from the target to the DSSD detector. Figure 7 shows the correlation between the neutron TOF and the detected charged particle's energy from the LENZ data (top) in 2016, in comparison with the MCNP simulation (bottom).

The reaction channel labeled as  $^{16}\text{O}(n, \alpha_0)$  in Fig. 7 is reconstructed assuming the reaction  $Q$  value of  $-2.2$  MeV and the  $^{16}\text{O}(n, \alpha_2 + \alpha_3)$  reactions assuming a reaction  $Q$  value of approximately  $-6.0$  MeV, consistent with the average between the second and third excited states in  $^{13}\text{C}$ . Since this solid oxygen target (Ta<sub>2</sub>O<sub>5</sub>) is not mono-elemental, beam-induced backgrounds were directly measured using a Ta blank target. With the 71-μm-thick DSSD, protons stop at about 2.5 MeV and punch through above this energy, showing no overlapping with  $\alpha$ 's above 2 MeV. The protons from  $^1\text{H}(n, p)$  were caused by the vacuum window made of Kapton foils in the entrance and exit ports in LENZ. The dominant background was due to neutrons scattering off the vacuum window and the thick Ta backing, then making reactions of  $(n, p)$ ,  $(n, d)$ ,  $(n, \alpha)$ , etc. in DSSDs, with the signature being the

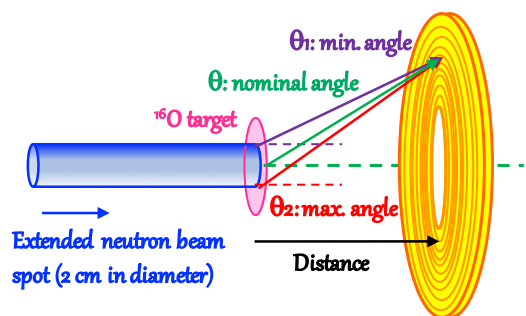


FIG. 6. Diagram to describe the angle determination in DSSDs for the experimental configuration of the 2016 and 2017 data sets. The beam spot size was 2 cm in diameter, therefore the actual angle per each annular segmentation in DSSDs ranges from  $\theta_1$  minimum angle to  $\theta_2$  maximum angle, instead of the nominal angle  $\theta$ .

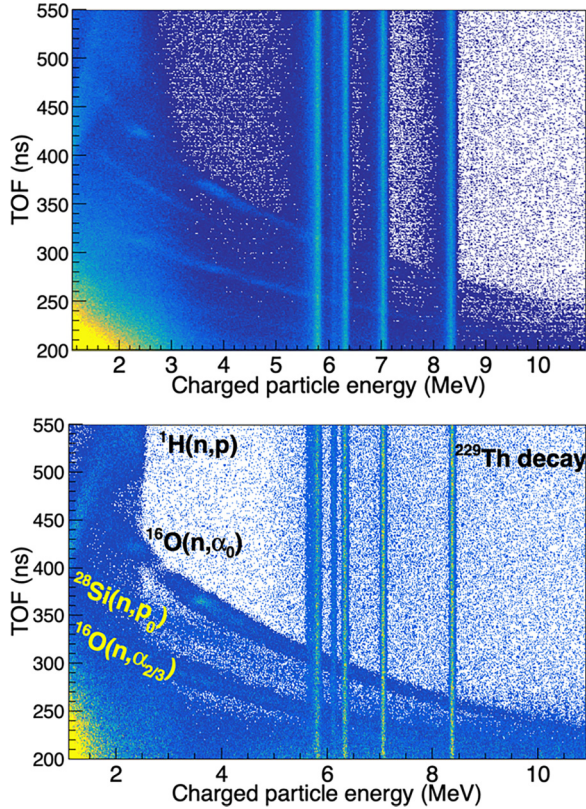


FIG. 7. Measured neutron's TOF relative to the  $\gamma$  flash vs the detected charged particle's energy (top) and the MCNP calculation for the 71- $\mu\text{m}$ -thick DSSD detector for the 2016 LENZ setup (bottom). In the MCNP calculation, the Th-229 source rate is overlaid with an arbitrary normalization to reproduce the LENZ data.

$^{28}\text{Si}(n, p)$  reaction, as shown in Fig. 7. The observed yield due to  $^{28}\text{Si}(n, p)$   $^{28}\text{Al}$  does not interfere with the extraction of the  $^{16}\text{O}(n, \alpha)$  cross sections; however, the kinematic curve from  $^{28}\text{Si}(n, \alpha)$  lies close to that of  $^{16}\text{O}(n, \alpha_0)$ , therefore these contributions are subtracted using the data of the blank Ta measurement.

### E. Forward propagation analysis using MCNP postprocessing

While MCNP has been widely benchmarked for calculating neutronics with high fidelity in various applications, the charged-particle transport was rarely validated with experimental data. With the progress in `mcnp6@` [51], we investigated the forward propagation analysis for neutron-induced charged particle emitting reaction data taken at LANSCE. We developed a postprocessing tool using the MCNP particle track (PTRAC) output to simulate charged particles' tracks following neutron-induced reactions at the LENZ instrument in flight path 15R, and compared with the LENZ data. The adequacy and completeness of the current neutron-induced charged particle emitting reaction evaluation in ENDF/B-VIII.0 for the isotopes of interest was benchmarked against the independent LENZ data using this postprocessing tool in the previous work [52]. In addition, we performed the validation of MCNP simulations for

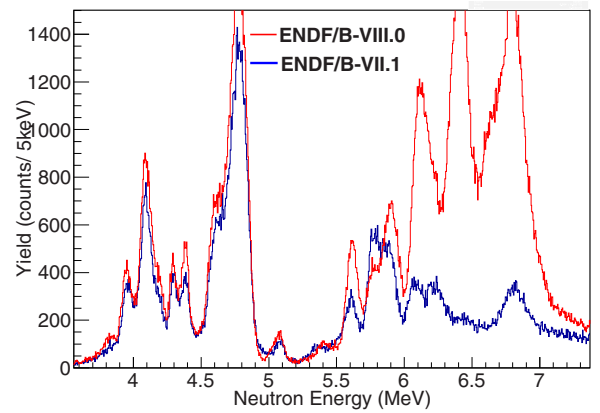


FIG. 8. MCNP simulations using the ENDF/B-VII.1 and ENDF/B-VIII.0 evaluations for the 2016 LENZ setup on the 71- $\mu\text{m}$ -thick DSSD. Although the nominal angles were defined as  $31^\circ$ – $38^\circ$ , the simulated actual angles covered  $30^\circ$ – $44^\circ$ .

spallation physics and neutronics at WNR by including the high-precision metrology survey of T4, the shutter, the beam defining collimation, LENZ, and the flight path. Detailed neutron spatial tallies and transport were well reproduced in beam imaging and neutron flux measurements at WNR flight paths [53].

As the most dominant background, neutron scattering can be corrected by measuring the yield with a blank target and subtracting it from the yield with a reaction target. This could result in up to a twofold beam time to meet the required precision. Investigating detector response functions using Monte Carlo methods like GEANT or MCNP could help reduce systematic and statistical uncertainties without directly measuring backgrounds for each reaction. Once the background (time dependent and random) is well characterized and the simulation is validated against reference measurements, yield simulations can be used to test different input nuclear libraries by reproducing experimental yields, as in the forward propagation analysis. Figure 8 demonstrates the sensitivity of different evaluations for the case of 2016 LENZ setup as simulated for experimental yields. In this work, MCNP simulations used the WNR neutron spectrum at 1–20 MeV and ENDF/B-VIII.0 as a default library, unless a different library is specifically mentioned.

The simulation was also used to estimate the angular smearing between “nominal” angles and “true” angles. The top panels in Fig. 9 show the 16 individual rings’ “nominal” angle determination as described in Fig. 6 and the bottom panels are the simulated angular responses with each color showing a group of four rings combined. In panel (c), the large angular broadening includes contributions from the  $\alpha$ 's angular straggling in the target and DSSD's dead layer, the extended beam spot of 2 cm in diameter, the distance between the target and DSSD, and the finite area of each ring. In this case, the dominant contribution was due to the extended beam spot size and the close geometry between the target and DSSD. Here, nonlinear behavior of angular responses between the experimentally determined “nominal” angle and the “true” emitting angle was observed in the 2016/2017

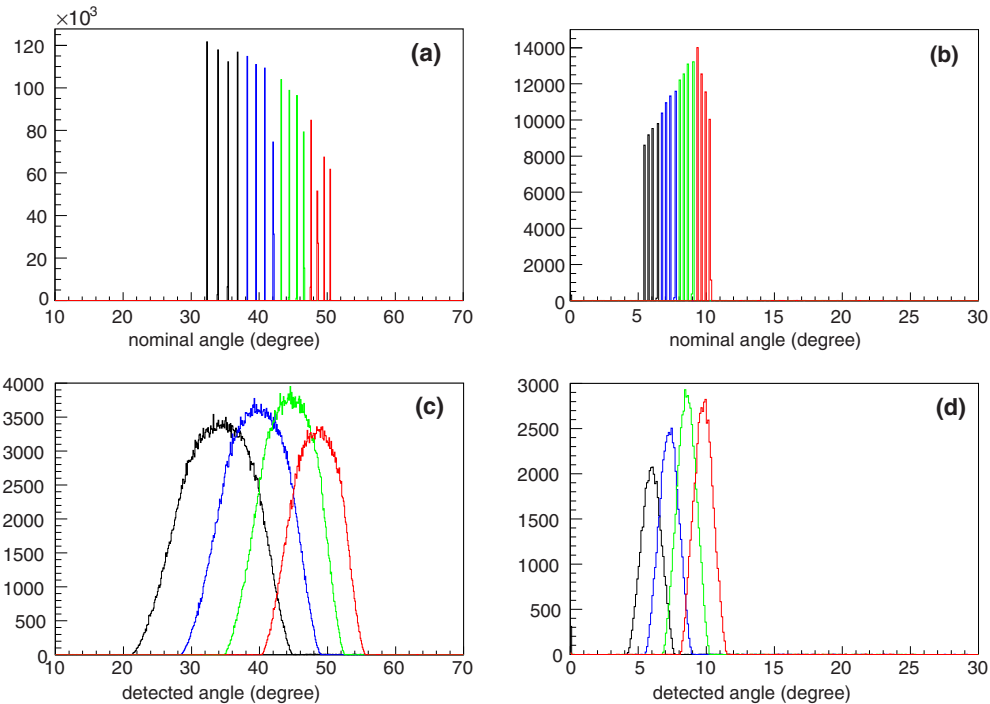


FIG. 9. MCNP simulations using ENDF/B-VIII.0 for (a,c) the 2016 experimental configuration with the detector located 3.9 cm from the target and the beam size of 1 cm in radius and (b,d) the 2021 experimental configuration with the detector located 25 cm from the target and the beam size of 0.5 cm in radius. (a,b) show nominal angles for individual 16 annular segmentations as described in Fig. 6 and (c,d) show detected angles,  $(\theta_2 - \theta_1)$ , of which four annular segmentations are combined into each colored group.

experimental configurations. As demonstrated in panel (d), the smaller beam spot and the longer distance between the target and DSSD suggested great improvement for experimental broadening, being less than 10%, and linearity with the nominal angular distribution was achieved when compared with panel (b). Finally, Fig. 10 shows the neutron-energy resolution function obtained from LENZ data to be applied for evaluated nuclear libraries for direct comparison with realistic experimental resolutions as LENZ data.

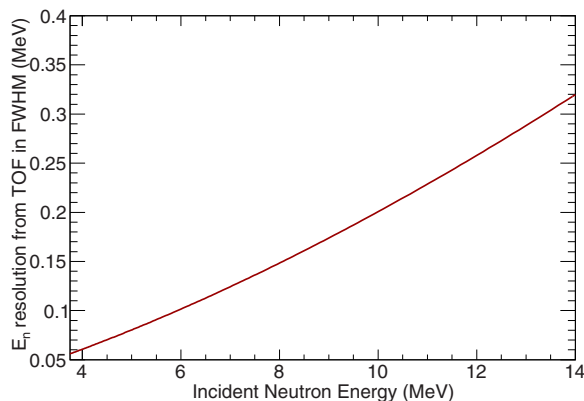


FIG. 10. Neutron-energy resolution function in full width at half maximum (FWHM) shown in MeV. This energy resolution function was applied for evaluated cross sections to compare with both 2017 and 2021 LENZ data.

### E. $^{16}\text{O}(n, \alpha)$ reaction measurements in 2021

Based on the results in the 2016/2017 data, the 2021 experimental configuration was optimized to reduce neutron scattering background and angular broadening with a goal of direct application for  $R$ -matrix analyses. First, the vacuum window material was replaced from the 75- $\mu\text{m}$ -thick Kapton ( $\text{C}_{22}\text{H}_{10}\text{N}_2\text{O}_5$ ) to the 125- $\mu\text{m}$ -thick aluminum foil. Second, an additional sweeper permanent magnet was installed right after the beam defining collimation to deflect any secondary charged particles from entering into LENZ as reduction in any further backgrounds due to  $(p, p')$ ,  $(d, d')$ ,  $(t, t')$ , etc. Third, new anodized targets with two different thicknesses of 350 and 500 nm were fabricated on thinner Ta backings from 125  $\mu\text{m}$  to 3  $\mu\text{m}$ . Lastly, the beam spot size was reduced from 2 cm to 1 cm in diameter, which resulted in better angular resolutions, but with a fourfold reduction in neutron flux at target.

The overall improvement including background reduction is contrasted in the 2021 LENZ simulation of Fig. 11(a), while Fig. 7 (bottom) shows the simulation for the 2016 LENZ configuration. Figure 11(b) is the LENZ data with the mylar target presenting prominent kinematic curves for the  $^1\text{H}(n, p)$  and  $^{12}\text{C}(n, \alpha_0)$  reactions, as the independent estimate for a neutron flux at the neutron energy range of 2.5–6 MeV. Figure 11(c) shows the LENZ data with the 350-nm  $\text{Ta}_2\text{O}_5$  target on the 3- $\mu\text{m}$ -thick Ta backing, making a large reduction on the ambient background compared with Fig. 7 (top). A small quantity of the  $^1\text{H}(n, p)$  reaction was measured due to moisture on a target frame. The  $^{238}\text{U}$  fission counter was



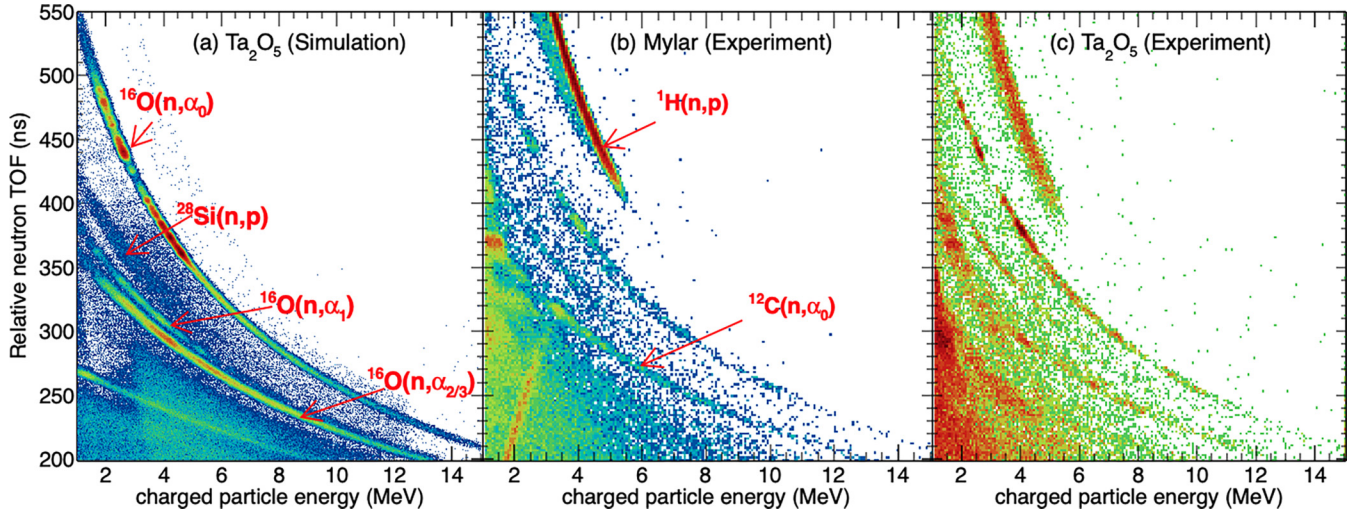


FIG. 11. (a) MCNP simulation of the neutron time of flight with respect to the  $\gamma$  flash vs the detected energy in DSSD using ENDF/B-VIII.0 for the 2021 LENZ configuration with the  $\text{Ta}_2\text{O}_5$  target, (b) the 2021 LENZ data with a mylar ( $\text{C}_{10}\text{H}_8\text{O}_4$ ) target, and (c) the 2021 LENZ data with the  $\text{Ta}_2\text{O}_5$  target on a thin Ta backing substrate. The MCNP simulation and LENZ data are compared for the detector positioned 12.5 cm from the target. The relative neutron TOF in the vertical axis means the neutron TOF is with respect to the  $\gamma$  flash time arriving at the oxygen target.

used to continuously monitor the beam flux over the runs with different oxygen targets.

The yields used to determine the reaction cross sections represent a sum over multiple detector rings which subtend a particular angle range. To determine the uncertainty on the mean angle, the relative yields measured in each ring (proportional to the trend in the angular distribution) are used to weight and recalculate the mean angle. This angle is compared to the nominal angle that is determined by the geometrical mean angle of the detector (each ring weighted by  $\sin\theta$ ) and by the MCNP simulation of the detector setup. The variation is typically less than  $0.1^\circ$ . Examples of simulated angular acceptance functions are shown in Fig. 9. Preliminary tests were performed to assess the effect of convoluting the high resolution angular distributions from ENDF or from literature over the angular acceptance, and affect the average

differential cross section by 1–3%. This is mainly because the excitation functions change smoothly as a function of angle so the impact of convoluting the angular acceptance is not as significant of an effect as convoluting the energy resolution.

### G. Uncertainties

The absolute cross sections were determined by combining both methods, since the ratio method to  $^1\text{H}(n, \text{el})$  is only valid for forward angle measurements. Therefore, the cross sections measured at backward angles and with the detector positioned at +2.5 cm with only the  $\text{Ta}_2\text{O}_5$  target were deduced using the direct normalization method. We used the ratio method to constrain the overall normalization by comparing the yields obtained with the detector in the 12.5 cm position that were recorded with both targets. For this, the

TABLE II. Itemized uncertainties for the 2021 LENZ data.

Neutron silicon detector	Energy determination		0.7–1.2%
	energy resolution		0.85%
	Solid angle/detector efficiency	incl. angular convolution	1.4–4% [54]
Direct normalization	$\text{Ta}_2\text{O}_5$ target	Thickness/amount	3%
		Stoichiometry	0.5%
	Fission counter	$^{238}\text{U}$ deposit nonuniformity	5%
		$^{238}\text{U}(n, f)$ cross section	1.5%
		Statistical unc.	0.1%
Systematic uncertainty	Direct normalization	Backward angles or +2.5 cm det. position	6%
	Ratio method	$^1\text{H}(n, \text{el})$ cross section	0.4 (3)%
Systematic uncertainty	Ratio method	Geometric effects	1%
		PSD background analysis	2%
		Forward angles, $E_n < 6$ MeV	2.3%
Systematic uncertainty	Ratio + fission counter	Forward angles, $E_n > 6$ MeV	2.75%
	Statistical uncertainty	Per energy bin	Per angle



yields measured using the nominal Ta<sub>2</sub>O<sub>5</sub> thickness and neutron fluence measured with the fission monitor were consistent with the oxygen yields measured with the mylar target within 6% for the forward angle detectors, which in turn was consistent with the itemization of expected uncertainties for each component. The statistical uncertainty on the fission monitor was treated as negligible since there were more than  $2 \times 10^6$  counts in the ionization chamber over the energy range of interest during the course of the current measurement, with 0.1% uncertainty per neutron energy bin. Thus, the total systematic uncertainty for the backward angle coverage for which there is no direct ratio comparison is 6%, for the direct normalization method. The uncertainties are now summarized in Table II to add clarity to how the different methods are combined to determine the absolute differential cross sections.

The primary sources of uncertainty from this ratio method are the use of  $^1\text{H}(n, \text{el})$  as a reference standard [0.4(3)%] and the difference between the detector response from protons and  $\alpha$  particles, which was estimated to be about 1% from geometric effects and 2% due to the selection cuts used in the pulse shape analysis to reject background contributions. This is also informed by a Monte Carlo simulation that includes the detector geometry, target and detector dead-layer effects, the relative timing corrections between the different particles, and small perturbations to the geometry [54–56]. As a result, the final systematic uncertainty with this ratio method is determined to be 2.3% and applies to the data points up to 6 MeV at the forward angles. Above this energy, an additional 1.5% uncertainty is adopted for the shape of the  $^{238}\text{U}(n, f)$  reference cross section at these energies. Combining these ratio measurements with the conventional neutron flux monitoring using a fission counter was achieved to improve the final systematic uncertainty. Hence, the systematic uncertainty related to the overall normalization is approximately 2.75% for the forward angle data points above 6 MeV. Therefore, the total uncertainty for this measurement is dominated by the statistical uncertainty that includes the subtraction of background counts, which typically varies 7%–15% per energy bin at each angle around the peaks of the resonances.

### III. RESULTS AND DISCUSSIONS

Differential cross sections on  $^{16}\text{O}(n, \alpha_0)$  were obtained at the average angles of  $12^\circ$ ,  $18.5^\circ$ ,  $66^\circ$ ,  $135^\circ$ , and  $155^\circ$  in the center-of-mass system as shown in Fig. 12. Here we report the 2021 LENZ results, which benefited from improved statistical uncertainties and energy/angular resolution, and are derived relative to  $^1\text{H}(n, \text{el})$ , which is considered a neutron standard at these energies. However, the results from 2016/2017 are consistent with the 2021 results presented here.

Since the observed resonances are typically narrower than our experimental resolution, the cross sections depicted in Fig. 12 represent an average cross section over the neutron energy bin width and the energy resolution of the detection system given in Fig. 10. For simplicity, we make comparisons with calculated differential cross sections by smearing the calculated cross sections, as shown by the solid red lines in each panel of Fig. 12. The calculation shown in blue and

brown in the top two panels are an  $R$ -matrix calculation using the code EDAP<sub>90</sub> [26,27] based on the resonance parameters used to produce the ENDF/B-VIII.0 evaluation. In the bottom panel, the ENDF/B-VIII.0 cross section of  $(n, \alpha_0)$ , divided by  $4\pi$ , is shown to elucidate any prominent resonance contributions at backward angles that are not being reproduced by the calculated angular distributions. In all panels it is clear that the calculated angular distributions above 6 MeV do not reflect the current experimental cross sections; however, ENDF/B-VIII.0 did not include any experimental angular distribution information at these energies. Instead, only the scale of the total cross section was constrained by recent and past data. Below 6 MeV, the data are in good agreement with the calculation using ENDF/B-VIII.0, for which the angular distributions were derived primarily from the work of Walton *et al.* [13].

The resonances that we observe are in good agreement with those previously reported by Davis *et al.* [12] and Robb *et al.* [18]. The former directly measured  $(n, \alpha_0)$  total cross sections and reported excitation energies in  $^{17}\text{O}$ , whereas Robb reported potential spin-parity assignments using a two-level analysis based on their  $^{13}\text{C}(\alpha, n_0)$  angular distributions. For example, the 7.2-MeV resonance that represents a prominent peak in the total cross section is most apparent at backward angles, while the weaker resonance around 7.0 MeV is observed at forward angles. Figure 13 shows some of the partial differential cross sections, with respect to laboratory angles, in comparison with the data from Robb *et al.* The overall scale of our cross sections is slightly larger, but is in relatively good agreement with the Robb data. The trends of the angular distributions are also in good agreement, which further supports some of the resonance analysis discussed in that work. A more complete  $R$ -matrix treatment of the  $^{17}\text{O}$  system at high energies was discussed in the work of Heil *et al.* [19], whereas the  $R$ -matrix analysis incorporated into ENDF/B-VIII.0 was limited up to only 6.5 MeV. The bottom three panels of Fig. 13 once again demonstrate the potential improvements that could be made to ENDF/B-VIII.0 at energies above 6 MeV to better constrain the resonance parameters and obtain more accurate angular distributions using available experimental data.

Figure 14 (top) shows summed partial differential cross sections from populating the first three excited states in  $^{13}\text{C}$  at two different angles. The different shapes between the two angles indicate that the angular distributions are typically not consistent with an isotropic distribution. In addition, the differential cross section at  $57^\circ$  shows better agreement with the trend of the  $(n, \alpha_2)$  cross section, whereas the more forward angle data are in slightly better agreement with the trend of the  $(n, \alpha_3)$  cross section, indicating the potential differences in their relative contributions. The bottom panel of Fig. 14 reflects an average of the two differential cross sections, multiplied by  $4\pi$ . The results show good agreement in comparison to ENDF/B-VIII.0 for which the partial cross sections are derived from the integrated cross sections of  $(n, \alpha\gamma_1)$ ,  $(n, \alpha\gamma_2)$ , and  $(n, \alpha\gamma_3)$  by Nelson *et al.* [57]. For  $(n, \alpha_0)$  at  $E_n > 9$  MeV, there is no significant difference between the different releases of ENDF so the trend that we observe is in good agreement with all of them.

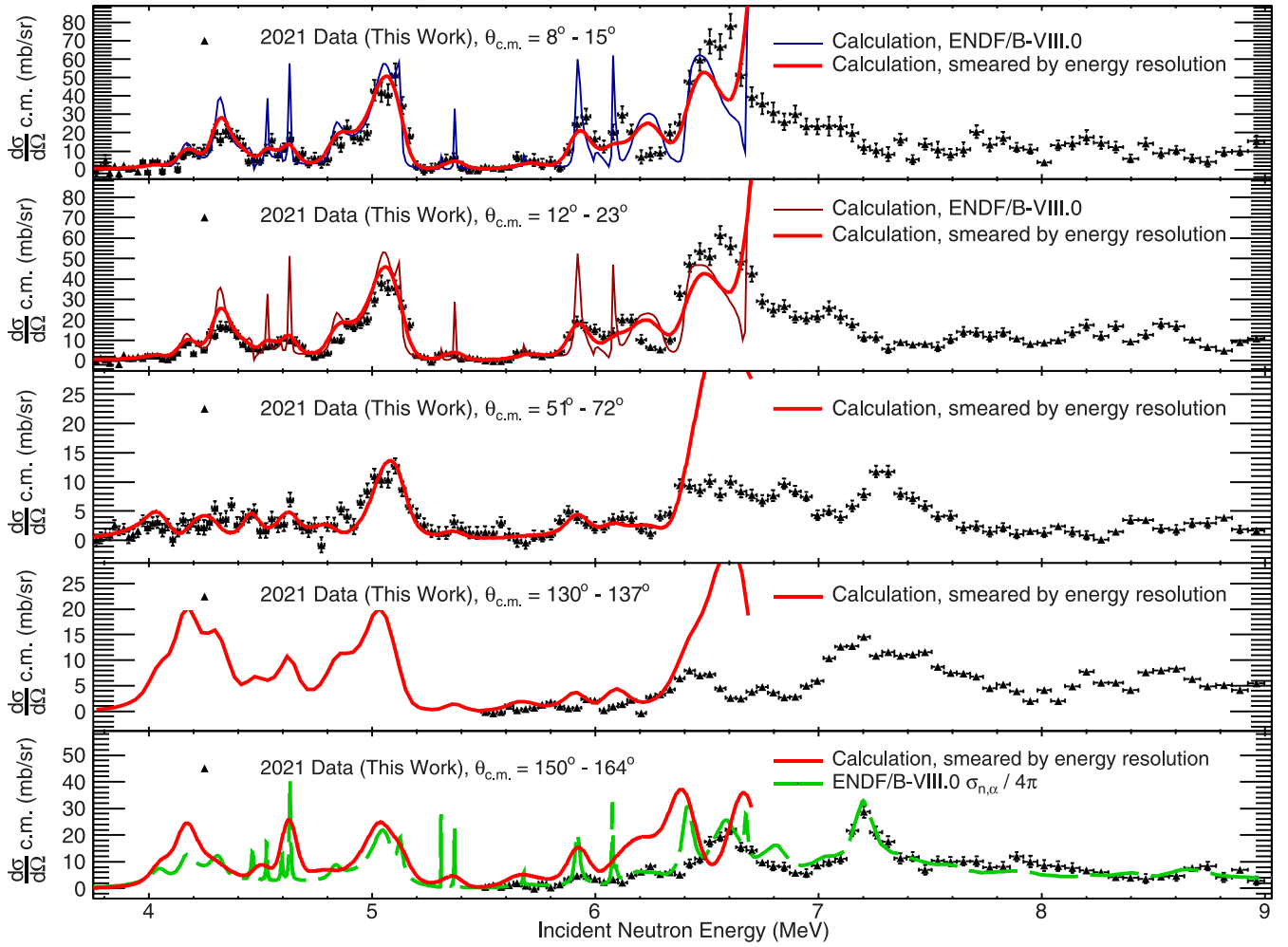


FIG. 12. Differential cross sections of  $^{16}\text{O}(n, \alpha_0)^{13}\text{C}$  from the 2021 LENZ data are compared with energy-averaged ENDF/B-VIII.0 values using the energy resolution function shown in Fig. 10.

Figure 15 presents the angle integrated partial cross sections derived from the differential cross sections in this work, where the shapes of the angular distributions have been constrained by the high resolution  $(\alpha, n_0)$  angular distributions from Walton (filled circles, up to 5.2 MeV) [13], Prusachenko (inverted triangles, up to 7.2 MeV) [14], and deBoer (open circles, up to 6.8 MeV) [25]. The various ENDF evaluations, smeared using the energy resolution function in Fig. 10 were compared with the partial cross section data. We find that the overall scale of our data is in better agreement with ENDF/B-VIII.0 than ENDF/B-VII.1 below 5.5 MeV; however, the results are also in good agreement with those of the original ENDF/B-VI.0 for which the inverse  $(\alpha, n_0)$  cross section in JENDL/AN-2005 [6] was derived.

#### IV. SUMMARY AND OUTLOOK

This work presents the direct measurement of differential cross sections from the  $^{16}\text{O}(n, \alpha)$  reaction over a broad range of incident neutron energy from 3.8 to 15 MeV at multiple angles, using solid oxygen targets and the LENZ

instrument. Experiments performed in 2016 and 2017 were used to validate the development of the MCNP and GEANT4 simulations of LENZ and the new postprocessing tool for the forward propagation analysis using different evaluation libraries. The 2021 LENZ data demonstrated drastic improvement on reducing systematic uncertainties and beam-induced backgrounds.

From the 2021 LENZ data, we report partial differential cross sections and partial cross sections in comparison with past experiments and evaluations. We compared the experimental data of  $^{16}\text{O}(n, \alpha_0)$  with energy-averaged ENDF/B-VIII.0, ENDF/B-VII.1, and JENDL/AN-2005 cross sections using the LENZ energy resolution function. Around 5 MeV, the scale of our experimental data is in good agreement with ENDF/B-VIII.0, ENDF/B-VI.8, and JENDL/AN-2005, but inconsistent with ENDF/B-VII.1. Over the entire measured energy range, the scale of our experimental data is in the best agreement with JENDL/AN-2005, which also gave the best agreement with the work of Febraro *et al.*, who measured the inverse  $^{13}\text{C}(\alpha, n)^{16}\text{O}$  reaction [24].

The current limitations with our measurement come from the setup, which is optimized for solid angle

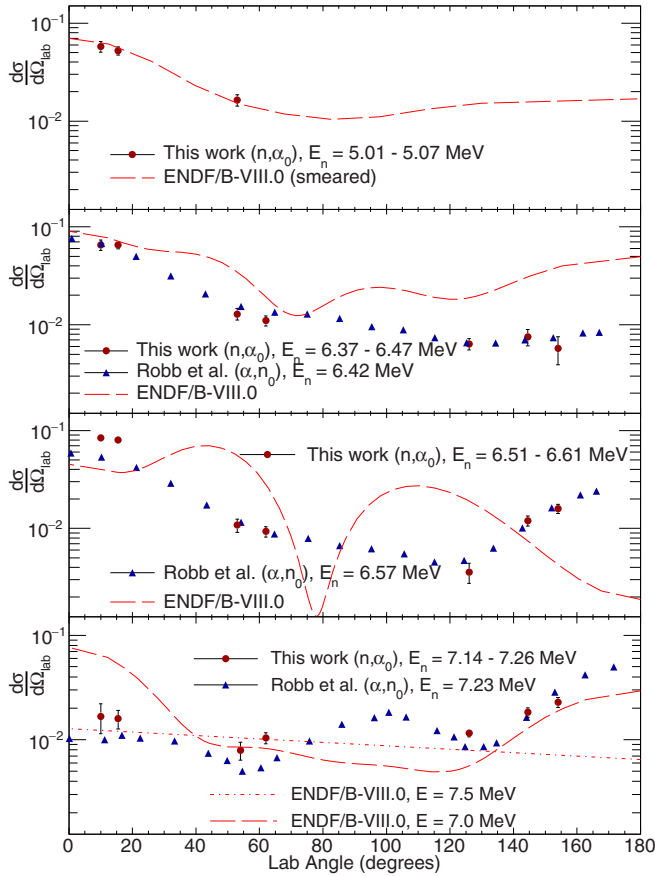


FIG. 13. Angular distributions of  $^{16}\text{O}(n, \alpha_0)^{13}\text{C}$  from the 2021 LENZ data are compared with Robb *et al.* and ENDF/B-VIII.0 at similar neutron energies.

coverage/efficiency instead of granularity or angular resolution in angular distributions. An increased neutron production at the WNR facility based on increased proton beam delivery from LANSCE would allow for a better compromise between detection yield and the angular coverage. The use of diamond detectors as an alternative to silicon detectors would also be beneficial since the neutron induced reactions on carbon have more negative  $Q$  values than the reactions on silicon, so background reactions around the  $Q$  value of interest are reduced. Diamond detectors also exhibit excellent timing properties with adequate detected energy resolution and capabilities of reject background contributions due to minimum ionizing particles using pulse-shape analysis. Another instrument to reduce energy and angular resolutions for measuring  $(n, \alpha)$  reactions could be a time-projection chamber (TPC), such as the Spatially Resolving Fission Tag (SREFT) [64], by tracing  $\alpha$ 's trajectories to reconstruct the exact reaction locus at an extended beam spot without compensating any solid angle coverage.

At the moment, however, measuring partial differential cross sections of the inverse  $^{13}\text{C}(\alpha, n_0)$  reaction to determine the  $(n, \alpha_0)$  direction appears to be the most straightforward method to obtain high resolution, in both energy and angle, cross sections. The work presented here provides an invaluable complementary dataset to the  $(\alpha, n)$  data. However, a

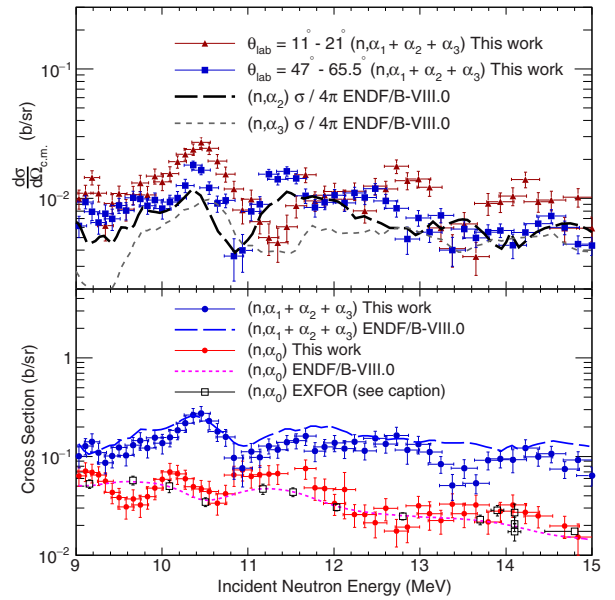


FIG. 14. Top: Partial differential cross sections of  $^{16}\text{O}(n, \alpha_1 + \alpha_2 + \alpha_3)$  measured at the average angles of  $15.5^\circ$  and  $57^\circ$  in the laboratory system. Bottom: Total cross sections populating the ground state and the first three excited states in  $^{13}\text{C}$ , after being multiplied by  $4\pi$ , are compared with ENDF/B-VIII.0. The experimental data from EXFOR for  $(n, a_0)$  that define the trend of ENDF at these energies are from Refs. [58–63]. The widths of horizontal error bars reflect FWHM of the neutron-energy resolution function shown in Fig. 10.

followup publication to that of Febraro *et al.* [24] with full angular distributions covering a broader energy range would provide an ideal data set to support  $R$ -matrix analyses like those performed by Heil *et al.* [19].

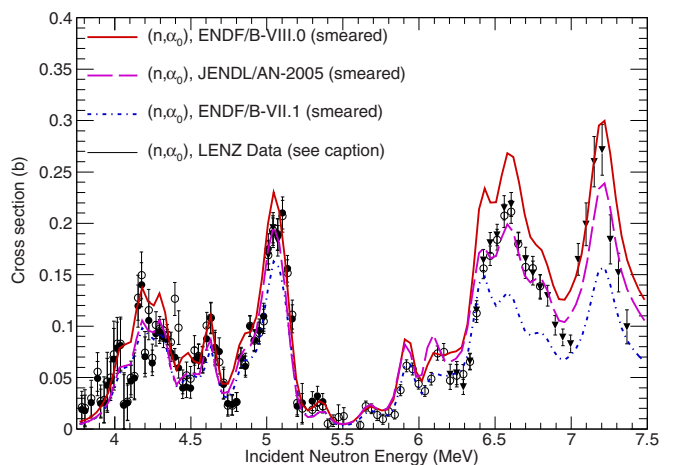


FIG. 15. The 2021 LENZ angle-integrated cross section of  $^{16}\text{O}(n, \alpha_0)^{13}\text{C}$  is compared with different releases of energy-averaged ENDF/B. Here, the shapes of the angular distributions have been constrained by the high resolution  $(\alpha, n_0)$  angular distributions from Walton (filled circles, up to 5.2 MeV) [13], Prusachenko (inverted triangles, up to 7.2 MeV) [14], and deBoer (open circles, up to 6.8 MeV) [25].



Although JENDL/AN-2005 gives the best agreement with the scale of our data at the measured energies, we suggest a full evaluation of the  $^{17}\text{O}$  system with new experimental data sets including not only angular distributions of  $^{16}\text{O}(n, \alpha_0)^{13}\text{C}_{\text{g.s.}}$  and recently available angular distributions of  $^{13}\text{C}(\alpha, n)$  [24], but also new total cross section measurements of  $^{13}\text{C}(\alpha, n)$  by the HeBGB Collaboration [65] with the energy independent detection efficiency. These partial differential cross sections are vital for improving the systematic uncertainties attributed to detection efficiency for total cross section measurements, previously reported by Bair and Haas and Harissopulos. Obvious deficiencies in the various evaluation libraries were found at energies above 6 MeV, due to outgoing angular distributions which were not sufficiently constrained by past experimental data or simply assumed an isotropic distribution. Finally, the data from this work can be used for validating the overall scale and relative shape of the differential cross sections in any new evaluations, due to the broad range of excitation energies that we measured simultaneously using the white neutron source at the WNR facility.

Although measurements of the inverse  $^{13}\text{C}(\alpha, n)$  reaction can currently provide higher energy and angle resolution, the capability of simultaneously measuring  $^1\text{H}(n, \text{el})$ , a neutron standard at the energy range of interest, is an added benefit of making neutron induced measurements.

#### ACKNOWLEDGMENTS

This work benefits from the LANSCE accelerator facility and is supported by the U.S. Department of Energy through the Los Alamos National Laboratory. Los Alamos National Laboratory is operated by Triad National Security, LLC, for the National Nuclear Security Administration of U.S. Department of Energy (Contract No. 89233218CNA000001). H.Y.L. acknowledges support from the Laboratory Directed Research and Development program of Los Alamos National Laboratory under Project No. 20130758ECR. We would like to thank Dr. J. Görres and Dr. E. Stech of the University of Notre Dame for providing great support on target characterization measurements at Notre Dame.

- 
- [1] CSEWG Collaboration, Evaluated Nuclear Data File ENDF/B-VI.8, <http://www.nndc.bnl.gov/endl>, 2001.
- [2] M. B. Chadwick *et al.*, *Nucl. Data Sheets* **112**, 2887 (2011).
- [3] D. A. Brown *et al.*, *Nucl. Data Sheets* **148**, 1 (2018).
- [4] A. J. M. Plompen *et al.*, *Eur. Phys. J. A* **56**, 181 (2020).
- [5] K. Shibata *et al.*, *J. Nucl. Sci. Technol.* **48**, 1 (2011).
- [6] T. Murata *et al.*, JAEA Research Report No. 2006-052, 2006 (unpublished).
- [7] G. Giorginis, V. Khryachkov, V. Corcalciuc, and M. Kievets, in *Proceeding of the International Conference on Nuclear Data for Science and Technology, ND2007* (2007), doi:10.1051/ndata:07481.
- [8] V. A. Khryachkov, I. P. Bondarenko, B. D. Kuzminov, N. N. Semenova, A. I. Sergachev, T. A. Ivanova, and G. Giorginis, *EPJ Web Conf.* **21**, 03005 (2012).
- [9] M. B. Chadwick *et al.*, *Nucl. Data Sheets* **118**, 1 (2014).
- [10] M. B. Chadwick *et al.*, *Nucl. Data Sheets* **148**, 189 (2018).
- [11] EXFOR: Experimental Nuclear Reaction Data, N. Otuka *et al.*, *Nucl. Data Sheets* **120**, 272 (2014); <https://www-nds.iaea.org/exfor/exfor.htm>
- [12] E. A. Davis *et al.*, *Nucl. Phys.* **48**, 169 (1963).
- [13] R. B. Walton *et al.*, *Phys. Rev.* **107**, 1065 (1957).
- [14] P. S. Prusachenko, T. L. Bobrovsky, I. P. Bondarenko, M. V. Bokhovko, A. F. Gurbich, and V. V. Ketlerov, *Phys. Rev. C* **105**, 024612 (2022).
- [15] J. K. Bair and F. X. Hass, *Phys. Rev. C* **7**, 1356 (1973).
- [16] K. K. Sekharan *et al.*, *Phys. Rev.* **156**, 1187 (1967).
- [17] S. Harissopulos, H. W. Becker, J. W. Hammer, A. Lagoyannis, C. Rolfs, and F. Strieder, *Phys. Rev. C* **72**, 062801(R) (2005).
- [18] A. D. Robb *et al.*, *Nucl. Phys. A* **147**, 423 (1970).
- [19] M. Heil *et al.*, *Phys. Rev. C* **78**, 025803 (2008).
- [20] M. T. Pigni and S. Croft, *Phys. Rev. C* **102**, 014618 (2020).
- [21] G. F. Ciani, L. Csedreki, D. Rapagnani, M. Aliotta, J. Balibrea-Correa, F. Barile *et al.*, *Phys. Rev. Lett.* **127**, 152701 (2021).
- [22] W. A. Peters, *Phys. Rev. C* **96**, 029801 (2017).
- [23] P. Mohr, *Phys. Rev. C* **97**, 064613 (2018).
- [24] M. Febraro, R. J. deBoer, S. D. Pain, R. Toomey, F. D. Becchetti, A. Boeltzig *et al.*, *Phys. Rev. Lett.* **125**, 062501 (2020).
- [25] R. deBoer, A. Gula, M. Febraro, K. Brandenburg, C. R. Brune, J. Görres *et al.*, *Phys. Rev. C* **106**, 055808 (2022).
- [26] G. M. Hale, *Nucl. Data Sheets* **109**, 2812 (2008).
- [27] G. M. Hale and M. W. Paris, *Nucl. Data Sheets* **123**, 165 (2015).
- [28] R. E. Azuma *et al.*, *Phys. Rev. C* **81**, 045805 (2010).
- [29] L. Leal *et al.*, *EPJ Nuclear Sci. Technol.* **2**, 43 (2016).
- [30] P. W. Lisowski *et al.*, *Nucl. Sci. Eng.* **106**, 208 (1990).
- [31] H. Y. Lee *et al.* (unpublished).
- [32] H. Y. Lee *et al.*, *EPJ Web Conf.* **122**, 05004 (2016).
- [33] H. Y. Lee *et al.*, *JPS Conf. Proc.* **14**, 020512 (2017).
- [34] R. C. Haight, in *Proceedings of the International Conference on Nuclear Data for Science and Technology, ND2007* (2007), doi:10.1051/ndata:07518.
- [35] F. B. Bateman, R. C. Haight, M. B. Chadwick, S. M. Sterbenz, S. M. Grimes, and H. Vonach, *Phys. Rev. C* **60**, 064609 (1999).
- [36] S. Kunieda *et al.*, *Phys. Rev. C* **85**, 054602 (2012).
- [37] Micron Semiconductor, <https://www.micronsemiconductor.co.uk>
- [38] Mesytec Technology, <https://www.mesytec.com>.
- [39] CAEN Electronic Instrumentation, <https://www.caen.it>
- [40] J. Allison *et al.*, *Nucl. Instrum. Methods A* **506**, 250 (2003).
- [41] P. Tsintari *et al.*, *Nucl. Instrum. Methods A* **1046**, 167666 (2023).
- [42] D. A. Vermilyea, *Acta Metall.* **1**, 282 (1953).
- [43] A. Best, M. Beard, J. Görres, M. Couder, R. deBoer, S. Falahat *et al.*, *Phys. Rev. C* **87**, 045805 (2013).
- [44] M. P. Seah *et al.*, *Nucl. Instrum. Methods B* **30**, 128 (1988).
- [45] M. P. Seah *et al.*, *Nucl. Instrum. Methods B* **30**, 140 (1988).
- [46] H. Costantini *et al.*, *Phys. Rev. C* **82**, 035802 (2010).
- [47] C. Rolfs, *Nucl. Phys. A* **217**, 29 (1973).
- [48] J. F. Ziegler, *Nucl. Instrum. Methods B* **219-220**, 1027 (2004).
- [49] S. A. Wender *et al.*, *Nucl. Instrum. Methods A* **336**, 226 (1993).
- [50] F. Tovesson *et al.*, *Nucl. Sci. Eng.* **178**, 57 (2014).

- [51] C. Werner, MCNP User's Manual, Code Version 6.2, Los Alamos National Laboratory Report No. LA-UR-17-29981, 2017 (unpublished).
- [52] H. I. Kim *et al.*, *Nucl. Instrum. Methods A* **963**, 163699 (2020).
- [53] B. DiGiovine *et al.*, *Nucl. Instrum. Methods A* **1013**, 165631 (2021).
- [54] S. A. Kuvin, H. Y. Lee, T. Kawano, B. DiGiovine, A. Georgiadou, C. Vermeulen, M. White, L. Zavorka, and H. I. Kim, *Phys. Rev. C* **102**, 024623 (2020).
- [55] S. A. Kuvin, H. Y. Lee, B. DiGiovine, A. Georgiadou, S. Mosby, D. Votaw, M. C. White, and L. Zavorka, *Phys. Rev. C* **104**, 014603 (2021).
- [56] S. A. Kuvin, H. Y. Lee, B. DiGiovine, C. Eiroa-Lledo, A. Georgiadou, M. Herman *et al.*, *Phys. Rev. C* **105**, 044608 (2022).
- [57] R. O. Nelson *et al.*, *Nucl. Sci. Eng.* **138**, 105 (2001).
- [58] D. Dandy, J. L. Wankling, and C. J. Parnell, Atomic Weapons Research Establishment Aldermaston Reports No. 60/68, UK, 1968 (unpublished).
- [59] I. Sick, E. Baumgartner, P. Huber, and Th. Stammbach, *Helv. Phys. Acta* **41**, 573 (1968).
- [60] T. Sanami, M. Baba, K. Saito, and N. Hirakawa, *Nucl. Instrum. Methods A* **440**, 403 (2000).
- [61] H. J. Brede, M. Moerike, B. Schuerenberg, G. Staudt, and F. Weng, *Z. Phys.* **245**, 1 (1971).
- [62] M. Bormann, D. Kaack, V. Schroder, W. Scobel, and L. Wilde, *Z. Phys.* **258**, 285 (1973).
- [63] W. N. McDicken and W. Jack, *Nucl. Phys.* **88**, 457 (1966).
- [64] K. T. Schmitt, Spatially REsolved Fission Tag (SREFT) - a low-mass TPC, Los Alamos National Laboratory Technical Report No. LA-UR-18-24582, 2018 (unpublished)
- [65] K. Brandenburg, G. Hamad, Z. Meisel, C. R. Brune, D. E. Carter, T. Danley, J. Derkin, Y. Jones-Alberty, B. Kenady, T. N. Massey, S. Paneru, M. Saxena, D. Soltesz, S. K. Subedi, and J. Warre, *J. Instrumentation* **17**, P05004 (2022).